https://doi.org/10.5194/egusphere-2026-1678
Preprint. Discussion started: 8 May 2026

Modeling the refractive index profile n(z) of polar ice for ultra-high energy neutrino experiments

Kenneth Couberly[1], Dave Besson[1], and ARA Collaboration[+]

[1]Dept. of Physics and Astronomy, University of Kansas, Lawrence, KS 66045
[+]A full list of authors appears at the end of the paper

Correspondence: Kenneth Couberly (kcouberly@ku.edu) and Dave Besson (zedlam@ku.edu)

Abstract. We have developed an *in-situ* index of refraction profile n(z) for cold polar ice, using the transit times of radio signals broadcast from an englacial transmitter to 1-5 km distant radio-frequency receivers, deployed at depths up to 200 m. For propagation through a non-uniform medium, Maxwell's equations generally admit two ray propagation solutions from a given transmitter, corresponding to a direct path (D) and a refracted or reflected path (R); the measured D vs. R timing differences (dt(D,R)) are determined by the refractive index profile. We constrain n(z) near the South Pole, where the Askaryan Radio Array (ARA) neutrino observatory is located, by simulating D and R ray paths via ray tracing and comparing simulations to measured dt(D,R) values. We demonstrate that our dt(D,R) timing data strongly favors a glaciologically-motivated three-phase densification model rather than the single exponential scale height models typically employed by in-ice radio neutrino detectors. Effective volume simulations for a detector of ARA station antenna depths yield a 14 % increase in neutrino sensitivity over a neutrino energy range of $10^{18} - 10^{21}$ eV using the three-phase model compared to the single exponential.

1 Introduction

Ultra-High Energy Neutrino (UHEN) experiments such as the Radio Neutrino Observatory in Greenland (RNO-G), the Askaryan Radio Array (ARA) at the South Pole, and the proposed IceCube Gen-2 experiment seek to extend the energy window of observed neutrinos beyond the MeV (typical of solar neutrinos) and PeV scales (astrophysical, as observed by IceCube) to >PeV ('cosmogenic') energy scales (Aguilar et al., 2022; Allison et al., 2016; Aartsen et al., 2021). Radio detection provides a cost-effective method for achieving large sensitive neutrino target volume, as radio signals propagate significantly farther in ice compared to optical signals. A major motivation of UHEN experiments is to complement observations of ultra-high energy charged cosmic rays (UHECR) from distant astronomical sources. UHEN are emitted following collisions of UHECR with matter or the Cosmic Microwave Background. Due to their lack of charge and small cross-section, neutrinos are able to propagate undeflected through obstacles otherwise opaque to gamma or cosmic rays. However, these same weakly interacting characteristics render observation difficult.

Radio propagation in ice, over kilometer-long distance scales, is essential for the radio neutrino experiments. Since the expected neutrino flux sharply decreases with increasing energy, radio neutrino experiments must scan large volumes for long exposure times to achieve measurable neutrino event rates. Simulations which incorporate models of the complex-valued radio-

https://doi.org/10.5194/egusphere-2026-1678
Preprint. Discussion started: 8 May 2026

frequency ice permittivity are used to estimate the sensitivity of UHEN experiments. The real part of the complex permittivity dictates the ray path followed by radio signals, from interaction point to receiver, while the imaginary part quantifies signal absorption in-ice. Given the non-magnetic nature of ice, the permittivity relates directly to the refractive index profile through $n = \sqrt{\epsilon_r}$ where ϵ_r is the real part of the ice permittivity. Since the overburden in the upper ∼100-150 m increases with depth, UHEN experiments assume a depth-dependent refractive index. For a given receiver, the depth-dependent refractive index profile generates, by Fermat's Least Time Principle, curved rather than rectilinear ray trajectories. This ray-bending also results in a 'shadowed' volume within which neutrino interactions will be inaccessible to a given receiver - this loss of sensitivity is increasingly important for large horizontal displacements and shallow receivers. As the depth of deployed receivers decrease, the extent of the shadowed zone is an increasingly important determinant of the visible neutrino interaction volume, and therefore the number of detected neutrinos.

The simplest ansatz for the refractive index profile is one that follows a single exponential dependence on depth, as expected for a self-gravitating fluid. Glaciological studies of ice density as a function of depth, however, suggest that densification occurs in multiple stages (Herron and Langway, 1980; Stevens et al., 2020; Salamatin et al., 1997). Using ARA receiver timing data obtained in response to a pulser lowered into the ice, we have tested a piece-wise function separated into these 3 stages against a simpler one-stage or two-stage exponential model.

2 Ice Densification and the Refractive Index

Our model assumes a linear dependence of refractive index on density (Robin et al., 1969). According to Sorge's Law (Bader, 1954), density is constant over time at a given depth, assuming constant snow accumulation and temperature. (In reality, the snow accumulation and temperature conditions are not constant, which leads to density fluctuations; in what follows, we neglect such effects, as well as the possible effect of impurities.) In a scale-height model, the densification rate of snow is taken to be proportional to the change in pressure due to the weight of the snow overburden, leading to the exponential form

$$\rho(z) = \rho_f - b_0 e^{Cz} \quad (1),$$

where ρ_f is the density of deep ice, $\rho_f - b_0$ is the density of snow at the surface, and C is a proportionality constant prescribed by the densification rate.

Theoretical and empirical models of ice density as a function of depth, however, prescribe two boundaries that affect the ice densification rate as $\rho(z)$ crosses density thresholds (Salamatin et al., 1997; Lipenkov et al., 1997). The (better-studied) first boundary at ∼550 kg/m^3 (Herron and Langway, 1980) separates the snow and firn regions, and occurs at depths of ∼15m and ∼20m for Summit and South Polar ice, respectively (Stevens et al., 2020). A second boundary separates the firn and bubbly ice regions. The ice is considered to be fully formed in the third region, but there still exist air pockets within the ice that reduce the overall density relative to ρ_f. These air pockets are crushed under greater pressure as depth increases, asymptotically reaching the ρ_f ∼920 kg/m^3 density of typical pure, deep ice at T=-30° C (Welling and Collaboration, 2024a). To account for changing densification rates in the separate regions, the form of Eqn. (1) is modified to a piecewise function where:

https://doi.org/10.5194/egusphere-2026-1678
Preprint. Discussion started: 8 May 2026

$\rho < \rho_1 : \rho(z) = \rho_f - b_0 e^{c_1 z}$,
$\rho_1 \leq \rho < \rho_2 : \rho(z) = \rho_f - b_0 e^{z_1(c_1 - c_2)} e^{c_2 z}$,
and $\rho \geq \rho_2 : \rho(z) = \rho_f - b_0 e^{z_1(c1-c2)} e^{z_2(c2-c3)} e^{c_3 z}$ (2)

to describe the 3 layers. In this parameterization, ρ_1 and ρ_2 are density boundary conditions with corresponding depths z_1 and z_2, b_0 is determined by the surface density and continuity at each boundary, and c_1, c_2 and c_3 are constants describing the densification rate in each depth region.

Figure 1 shows ice density data taken from a number of sites in Greenland. This density data approaches the asymptotic value and therefore includes measurements well into the expected bubbly ice region. We use a 550 kg/m^3 boundary between the snow and firn regions based on previous studies (Herron and Langway, 1980; Stevens et al., 2020), while the boundary between firn and bubbly ice is determined empirically by fitting the $\rho(z)$ data for the inflection point separating the intermediate and highest density regions, using the Levenberg–Marquardt fitting algorithm (Gavin, 2019). In this fitting procedure, the surface density, c_1, c_2, c_3, and the firn/bubbly ice boundary are taken as free parameters while the snow/firn boundary and asymptotic density are fixed at 550 kg/m^3 and 920 kg/m^3, respectively. Each data point from the compiled density data is weighted equally in this fit. Applying the fitting algorithm gives a 758 kg/m^3 boundary between the firn and bubbly ice regions which is used to determine the second depth boundary in Eqn. (2). Past studies of the snow/bubbly ice density boundary have used values from 800-830 kg/m^3 (Herron and Langway, 1980; Lipenkov et al., 1997). For the single exponential, the same fitting algorithm is used and only b_0 and c in Equation (1) are taken to be free parameters. This gives a best fit single exponential to the compiled data:

$\rho(z) = 920 - 548.5e^{-0.0241z}$ (3).

A 3 stage exponential fit using the form of Equation (2) gives:

$\rho < 550\ \mathrm{kg/m^3} : \rho(z) = 920 - 551.7e^{-0.0262z}$,
$550\ \mathrm{kg/m^3} \leq \rho < 758\ \mathrm{kg/m^3} : \rho(z) = 920 - 373.4e^{-0.0193(z-14.9)}$, and
$\rho \geq 758\ \mathrm{kg/m^3} : \rho(z) = 920 - 159.0e^{-0.0339(z-58.9)}$ (4).

2.1 Calculating refractive index from density

While there exists variation in the parameters for different sets of data, the linear relation assumed for n(ρ(z)) serves as a useful ansatz for the dielectric–specific-gravity relation (Kovacs et al., 1995), and is supported by studies at the Maudheim and McMurdo ice shelfs as well as studies of snow in Canada and Japan (Schytt, 1958; Evans, 1965; Cumming, 1952):

$n(z) = 1 + A\rho$(z) (5),

where ρ is the pure ice specific-gravity and A is a proportionality constant with units cm^3/g, and can be estimated from the constraint that deep, bulk ice has a refractive index corresponding to the measured value at a given site. At Summit Station, Greenland, n=1.778$\pm$0.006 , (Welling and Collaboration, 2024a, b) for deep bulk ice. Different fits to McMurdo ice shelf data give A values ranging from 0.840-0.858. The A value of 0.845 determined from the most recent McMurdo ice shelf study (Kovacs et al., 1995) also matches the conversion of the asymptotic ice density 920 kg/m^3 to the refractive index value n=1.778. We therefore use A=0.845 to convert SPICE core density to n(z) (see Section VI), to give: $n(z) = 1.778 - B_0 e^{Cz}$ (6), where

https://doi.org/10.5194/egusphere-2026-1678
Preprint. Discussion started: 8 May 2026

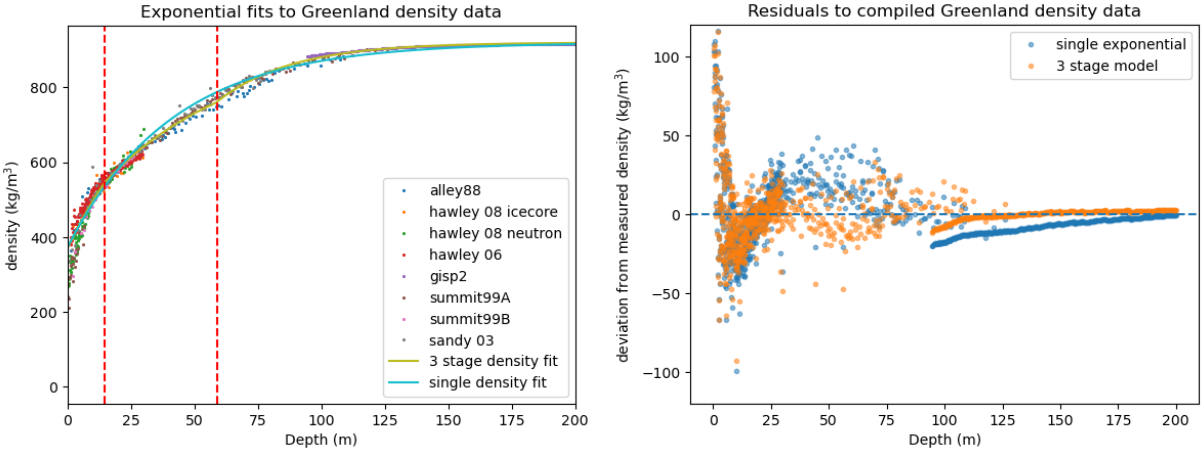

Figure 1. Equations (3) (single) and (4) (3 stage) parameterization fits to compilation of Greenland ice density data. Fixing the snow/firn boundary at 550 kg/m^3, the fit implies a firn/bubbly ice boundary of 758 kg/m^3. Red dotted lines (14.9 m, 58.9 m) indicate corresponding density boundaries. Density data have been taken from (Gow et al., 1997; Alley and Koci, 1988; Hawley and Morris, 2006; Hawley et al., 2008).

B_0 is $A \times b_0$ from Eqns. (5) and (1), respectively and C is constant, as in Eqn. (1). Applying the same density to refractive index conversion to Eqn. (2) gives a 3 stage refractive index model with the piecewise form:

$$z < z_1 : n(z) = 1.778 - B_0 e^{c_1 z},$$
$$z_1 \leq z < z_2 : n(z) = 1.778 - B_0 e^{z_1(c_1-c_2)} e^{c_2 z}, \text{ and}$$
$$z \geq z_2 : n(z) = 1.778 - B_0 e^{z_1(c_1-c_2)} e^{z_2(c_2-c_3)} e^{c_3 z} \quad (7).$$

In Eqn. (7), c_1, c_2, c_3 are exponential parameters to be determined by the fitting the model to timing data.

2.2 Experimental Layout

Analyzed ARA data discussed below are drawn from multiple (and often overlapping) combinations of transmitters and receivers, spanning in-ice transmitter depths of up to 1.5 km and horizontal trajectories of up to 5 km over a wide range of incidence angles. A map of the relevant radio-frequency instrumentation in the vicinity of South Pole is presented in Figure 2, showing the receiver stations relative to the radio-frequency transmitters.

3 Deep Pulser Data

A typical ARA station is shown in Figure 3; ARA consists of 5 such stations, denoted as 'A1'-'A5'. Each station consists of 4 boreholes at the vertices of a horizontal square, with an inter-string lateral separation of order 20 meters; each borehole contains a vertical string of radio receiver antennas. Each string consists of 2 horizontally polarized (Hpol) and 2 vertically polarized (Vpol) antennas, deployed at depths ranging from 170-200 m. This allows the stations to record both Hpol and Vpol

https://doi.org/10.5194/egusphere-2026-1678
Preprint. Discussion started: 8 May 2026

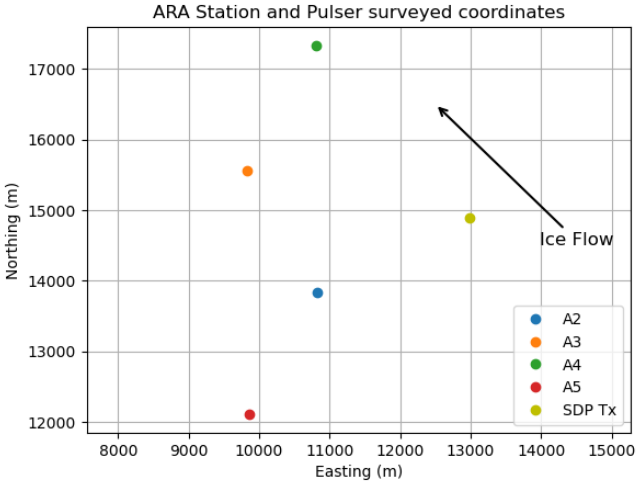

Figure 2. Surveyed coordinates (Easting, Northing) for ARA stations A2, A3, A4 and A5 for which timing data from the SPICE Deep Pulser (SDP) are analyzed.

signals, and thereby infer the polarization of a signal based on the relative amplitudes registered on the Hpol vs. Vpol antennas. Reconstruction of a source location is based on relative signal timings received by multiple antennas. Nearby (30–50 m away) englacial pulsers are used to calibrate channel positions. In our case, we are interested in not only the direct (D) signal arrival time, but also the refracted/reflected (R) signal arrival time from a distant transmitter.

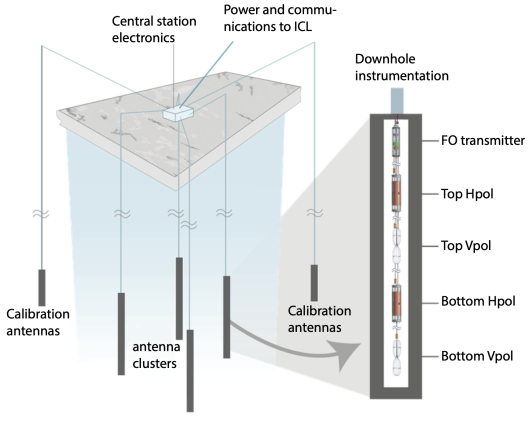

Figure 3. ARA station layout, comprising 16 antennas (8 Hpol and 8 Vpol) ranging from 170-200 m depths.

A waveform similar to that seen in Figure 4 is divided into its D and R components. The waveform is converted to a Hilbert envelope, and the timing of each peak is determined by fitting the Hilbert envelope of each peak to a Gaussian.

https://doi.org/10.5194/egusphere-2026-1678
Preprint. Discussion started: 8 May 2026

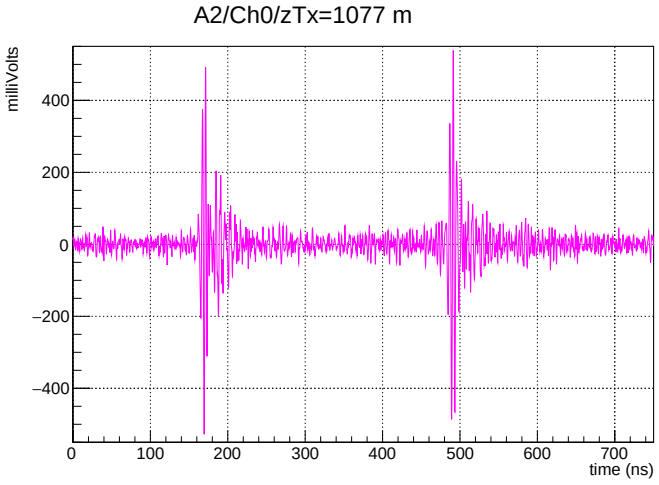

Figure 4. Typical waveform recorded during SDP transmitter run; Direct (earlier) and Refracted (later) pulses are evident in the Figure.

The dt(D,R) timing difference offers several advantages in calibration. In addition to being immune to single channel data acquisition signal transmission (aka 'cable delay') uncertainties, it also offers enhanced discrimination between different n(z) models due to the differences between the D and R optical paths (illustrated in Figure 5). The R ray path travels through ice well above the receiver antenna which allows for testing a greater range of depths for n(z). By contrast, nearby calibration pulsers only test n(z) over the limited depth range of the deployed ARA antennas. From a science perspective, since, to a first approximation, dt(D,R) depends linearly on the range to source location (discussed below), it can also be used as a powerful constraint in neutrino reconstruction, independent of conventional interferometric techniques to locate interaction points (Latif, 2020).

The South Pole Ice Core Experiment (SPICE) borehole was drilled to 1751 m over the 2014-2015 and 2015-2016 austral seasons with the purpose of collecting data to determine changes in atmospheric chemistry, climate, and biogeochemistry since the most recent [40 ka] glacial-interglacial cycle (Casey et al., 2014). Proximal (1-4 km from stations A2-A5 (Allison et al., 2020)) to the ARA stations, SPICE offers both density data and the opportunity for deep pulser timing measurements.

The SPICE deep pulser ('SDP') transmitter antenna was deployed into the SPICE borehole, and broadcast 1 pulse per second (pps) signals. Approximately 200 pulses are transmitted at each depth and averaged to calculate timing differences. Figure 4 shows a 64-event average waveform obtained from a deep pulser ('SDP') lowered into the SPICE borehole in Dec., 2018. Stations began receiving double pulse (D,R) signals once the transmitter emerged from the shadow zone (around a depth of 500–700m, depending on the receiver station) resulting in a dataset of dt(D,R) pulses recorded to z=1300 m. ARA stations recorded signal from the SDP over a range of 150-1000 MHz. A more detailed description of the SDP pulsing runs and received signals can be found in the literature (Allison et al., 2020). We use this dataset to constrain n(z) models.

https://doi.org/10.5194/egusphere-2026-1678
Preprint. Discussion started: 8 May 2026

4 Simulated Deep Pulser Signals

Ray paths originating at the SDP transmitter are simulated using the numerical ray tracer `RadioPropa` (Winchen, 2019), which calculates the two possible solutions (D and R), given source and receiver positions and an input n(z) model. Figure 5 shows the simulated ray paths from a 1300 m deep source to an ARA antenna. The D ray path travels only through the bubbly ice region while the R path travels through both the bubbly ice and firn regions of the 3 stage model.

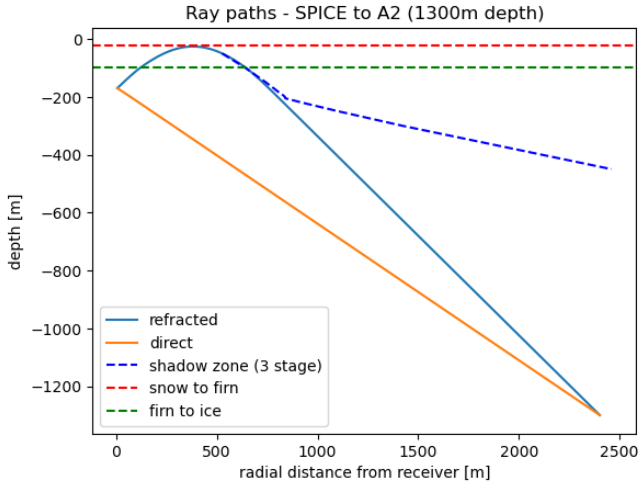

Figure 5. Simulated (using Eqn. (6)) direct and refracted ray paths from a 1300 m deep pulser in the SPICE borehole to channel 0 of ARA staton A2. Horizontal dotted lines depict the boundaries between regions of the 3 stage n(z) model. Shadow zone refers to the area above and to the right of the dashed blue line where pulses cannot be detected.

The ray tracing code `RadioPropa` is incorporated into `NuRadioMC`, a complete Monte Carlo simulation suite that can be used to simulate signal waveforms and determine the neutrino detection volume for a given radio neutrino detector configuration (Glaser et al., 2020). In addition to relative signal arrival times, the relative amplitudes of the D and R signals as well as frequency content can also be used to compare simulated waveforms to data. In what follows, we consider only timing information; amplitude analysis is currently underway.

5 Ice model results

To ensure the transmitter is well beyond the shadow zone, we measure dt(D,R) over the depth range from 700–1300 m for most stations. Typical horizontal separations are of order 1–5 km - in the case of A3, for example, the SPICE borehole is laterally displaced 3230 m. A sample A2 VPol waveform used for analysis is shown in Figure 4; in this case, the transmitter was located at a depth of 1077 m.

https://doi.org/10.5194/egusphere-2026-1678
Preprint. Discussion started: 8 May 2026

5.1 Fitting models to A2 dt(D,R) data

To assess the fidelity of our n(z) model, we use station A2 dt(D,R) data (selected on the basis of being the most-studied of the current ARA stations) as a 'training set' to extract, via χ^2 fit of simulation to data, numerical values for the required one-stage, two-stage, or three-stage n(z) constants (Eqns. (6) and (7)) and then fix those values for comparing data vs. simulations for the other stations. For all models, the surface parameter B_0 and the asymptotic refractive index 1.778 are fixed. For the multi-stage models, boundary depths z_1 and z_2 are determined using the SPICE core density data, and then fixed; density boundaries of 550 kg/m^3 and 758 kg/m^3 imply phase transition boundary depths of 20.5 m and 96.6 m, respectively. When converted using Eqn. (5), the surface density implies B_0=0.45.

The minimum χ^2 estimate is performed on 368 measured dt(D,R) data points from the SDP across the 8 VPol channels. The same minimum χ^2 estimate is performed for the 2 stage and 3 stage models with 2 and 3 free parameters for the additional c_2 and c_3 parameters for the models, respectively. The minimum χ^2 parameters for the 1 stage, 2 stage, and 3 stage models are presented in Table 1. The summed χ^2 per degree of freedom for these models are 406.5, 295.8, and 9.3, respectively. The higher χ^2 in the 1 stage and 2 stage n(z) model fits to A2 is a result of an inability of the models to fit dt(D,R) across a range of transmission depths. The resulting fitted 1 stage, 2 stage, and 3 stage model parameters are shown in Table 1.

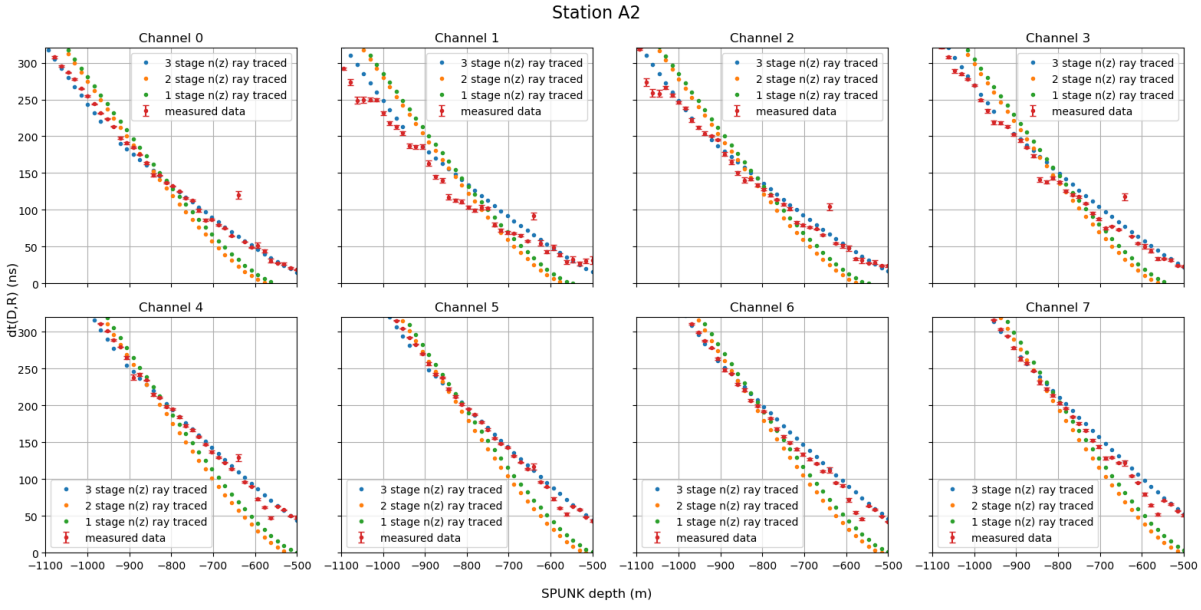

Figure 6. dt(D,R) for Eqn. (5), (6), and (7) compared to measured data for station A2. Models were fit to minimize χ^2 to data across channels shown, with parameters shown in Table 1.

https://doi.org/10.5194/egusphere-2026-1678
Preprint. Discussion started: 8 May 2026

n(z) model	c_1	c_2	c_3
1 stage	0.0146	N/A	N/A
2 stage	0.0165	0.0136	N/A
3 stage	0.0147	0.0112	0.0310

Table 1. Parameters of A2 dt(D,R) minimum χ^2 estimate for 1 stage, 2 stage, and 3 stage models.

5.2 Comparison to converted SPICE density data

We compare the 3 models to SPICE core density data converted to n(z) via Eqn. (5), with A=0.845. Figure 7 shows the 1 stage, 2 stage, and 3 stage A2 dt(D,R) parameterizations shown in Table 1. The residuals show the best-fit 3 stage model to the SPICE density data, particularly over the firn region between 20.5 m and 96.6 m. However, in the bubbly ice region (z$>$ 96.6 m), the 3 stage model typically exceeds the density-implied n(z), although this is also the regime for which the data statistics are smallest.

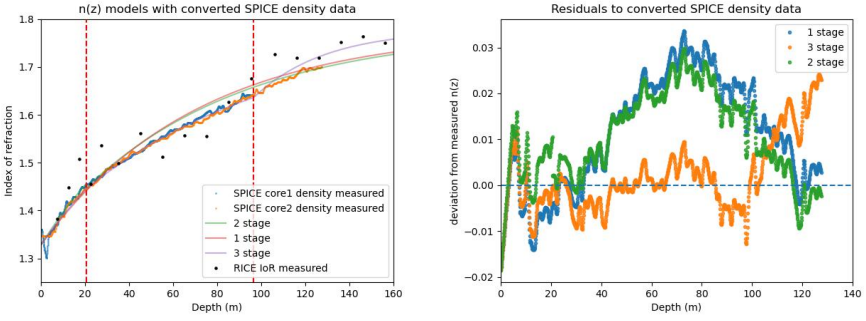

Figure 7. Density profiles corresponding to 1 stage, 2 stage, and 3 stage models (see Table 1) compared to converted SPICE core density data (Allison et al., 2020) down to 127 m depth. Deviation between the two SPICE core density measurements suggest an error of $\pm$ 0.005 in density-converted n(z) values. Residuals are shown relative to converted SPICE core density data.

5.3 Timing analysis for other ARA stations

Figure 8 shows the Δ dt(D,R) values for various depths of SDP broadcasts to ARA station A3 for the n(z) models corresponding to the 1 stage, 2 stage, and 3 stage parameterizations extracted from independent fits to A2 data, and shown in Table 1. 'Measured' times refer to dt(D,R) calculated using the arrival times of the D and R signals in double pulse waveforms similar to Figure 4; 'Simulated' times refer to dt(D,R) calculated from the D and R `RadioPropa`-prescribed ray paths, for given source and receiver locations. Shown in Figures 8–10 are Δdt(D,R) values as a function of SDP pulsing depth.

https://doi.org/10.5194/egusphere-2026-1678
Preprint. Discussion started: 8 May 2026

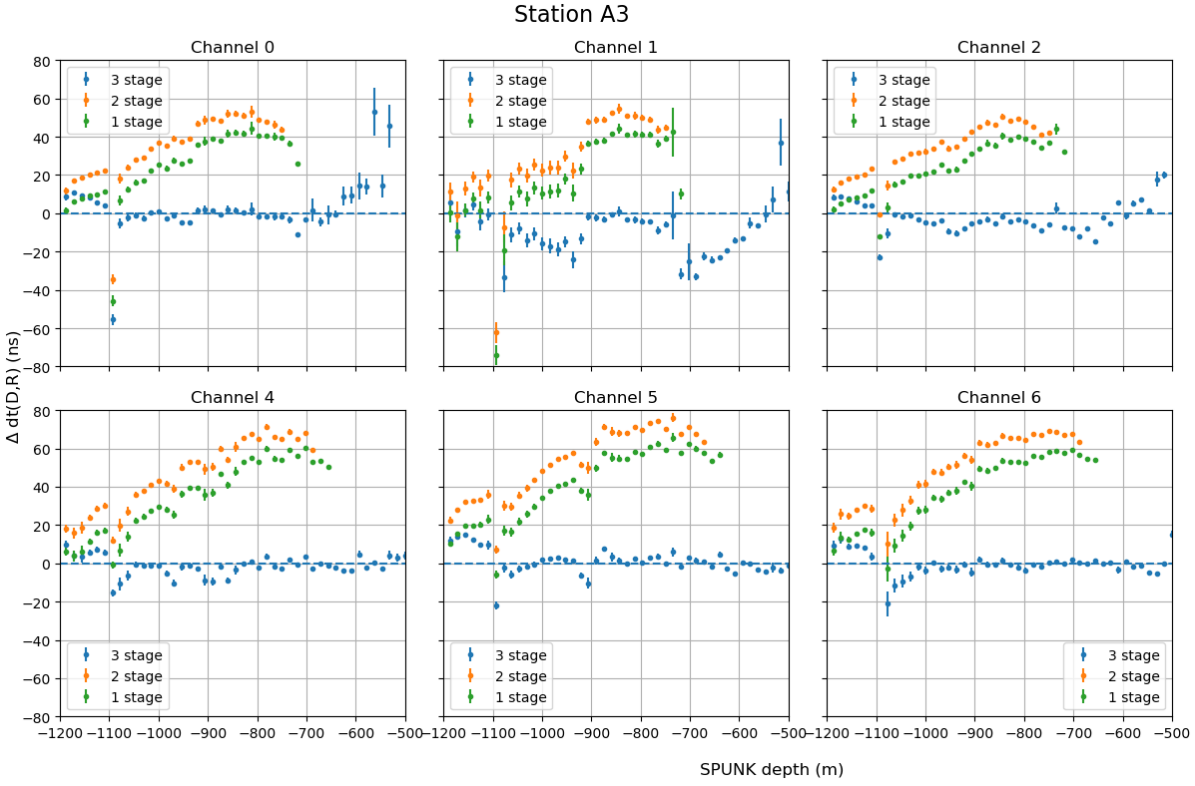

Figure 8. Δdt(D,R) for signals traveling from SDP to station A3 for Vpol channels. Shown are comparisons of simulated vs measured dt(D,R) for Eqn. (5), Eqn. (6), and Eqn. (7).

As illustrated in Figures 8 and 9, the 1 stage and 2 stage models show a trend for which measured dt(D,R) increases relative to simulated dt(D,R) at shallower depths. The discrepancy can be markedly reduced by using a 3 stage model, for which the c_3 parameter is increased in the bubbly ice region relative to the c parameter of the single exponential.

Station A5 is located 4165 m from the SPICE borehole, approximately 1 km further than the other stations. This larger lateral distance also results in an increased extent of the shadowed zone (see section VII), corresponding to dt(D,R) data only being measurable over a range of 850-1300 m source transmitter depth. Figure 10 shows the measured – simulated dt(D,R) results, comparing the different refractive index parameterizations for station A5. As with the A3 and A4 datasets, we use the c_3 parameter determined from A2 data and apply that value to the independent A5 dataset. The 1 stage and 2 stage models deviate further from the A5 data, which is improved using the 3 stage n(z) model. The 1 stage and 2 stage models also imply a shadow zone boundary deviating from measured data.

https://doi.org/10.5194/egusphere-2026-1678
Preprint. Discussion started: 8 May 2026

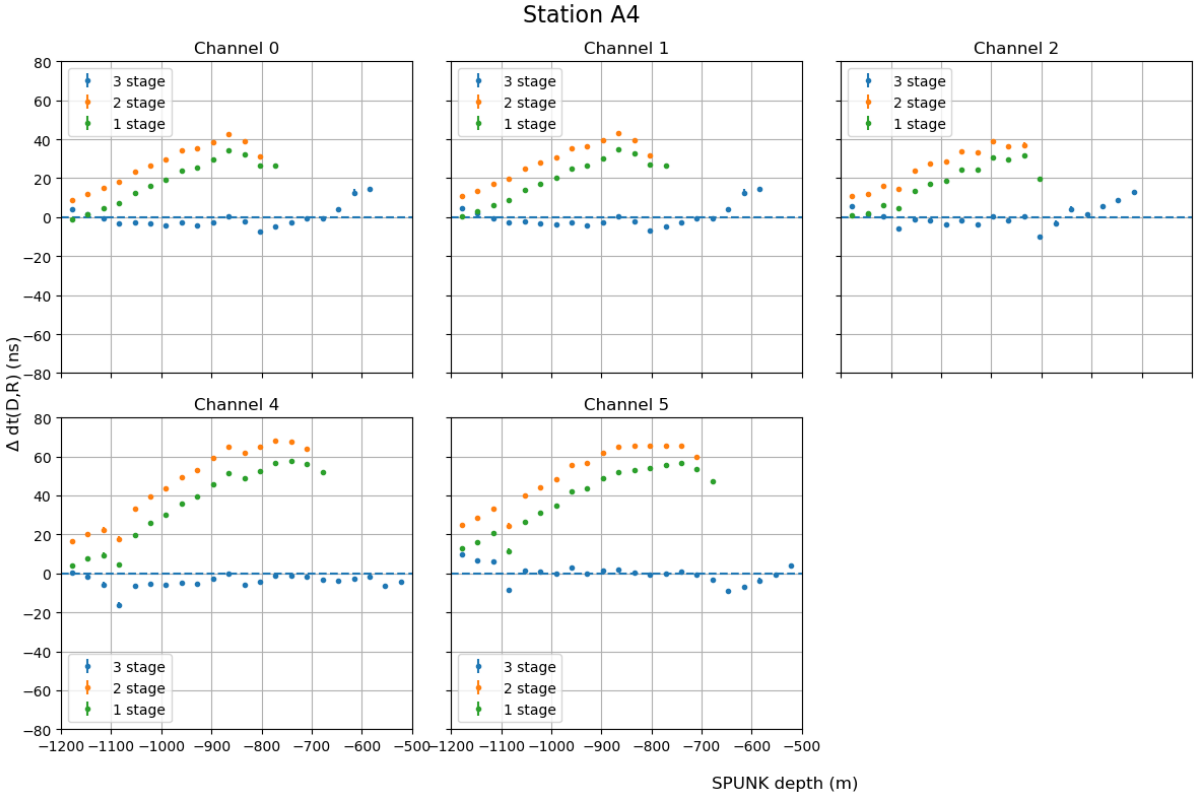

Figure 9. Δdt(D,R) for signals propagating from SDP to station A3.

6 Shadowed Zone

As a source moves further away laterally from a receiver or upwards to a shallower depth, dt(D,R) decreases. Eventually, as dt(D,R) approaches 0, the D and R signals seen in Figure 4 coalesce. Initially, this results in focusing that increases signal amplitude. However, beyond a certain point, corresponding to the shadow zone boundary, the bending of possible paths no longer allows signal to reach the receiver from the transmitter. An example of this would be a transmitter that lies above the blue dashed line shown in Figure 5 relative to the receiver. Since refraction is determined by the n(z) model, the shadowed zone, as well as the detected neutrino rate, both depend on n(z).

7 Impact on neutrino detection

Figure 11 illustrates how changes in the refractive index model affect the lateral extent of the shadow zone. Overall, we observe that the 3 stage model results in a more restricted accessible target volume for 100 m depth receiver deployments and correspondingly slightly decreased neutrino sensitivity. By contrast, Figure 12 compares effective volume simulations using

https://doi.org/10.5194/egusphere-2026-1678
Preprint. Discussion started: 8 May 2026

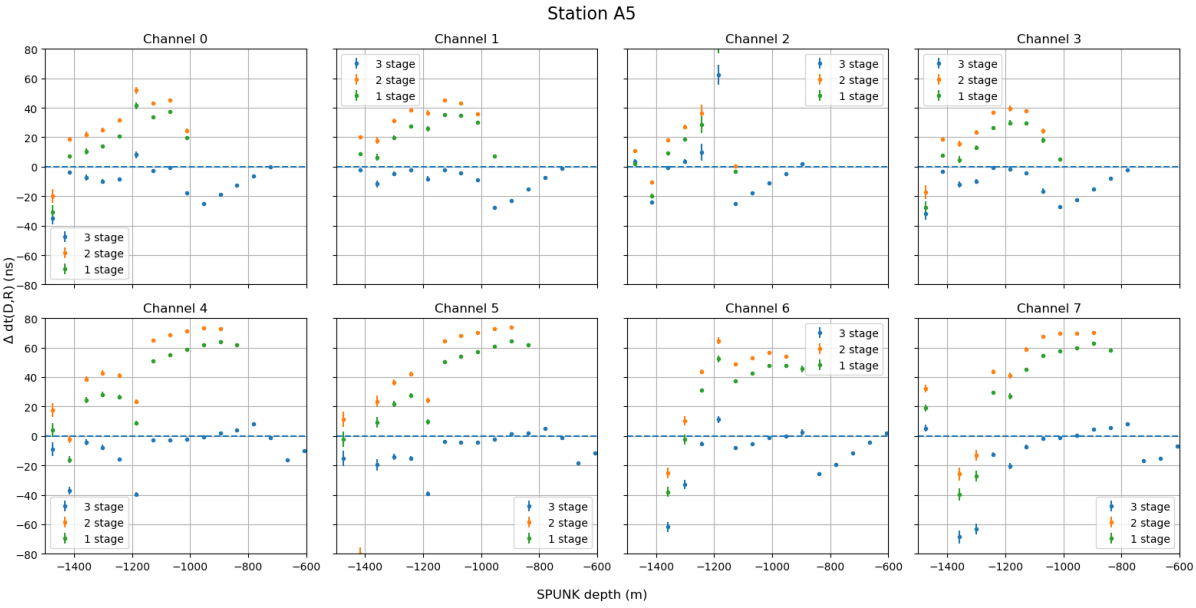

Figure 10. ARA station A5 Δdt(D,R), extracted using 1 stage, 2 stage, and 3 stage index of refraction models from Table 1. The refractive index parameterization from the 3 stage model improves the agreement relative to the 1 stage and 2 stage models as a function of SDP depth. A lack of simulated dt(D,R) solutions from the shadow zone of the models results in some 'missing' values at shallow SDP depths for the 1 stage and 2 stage models.

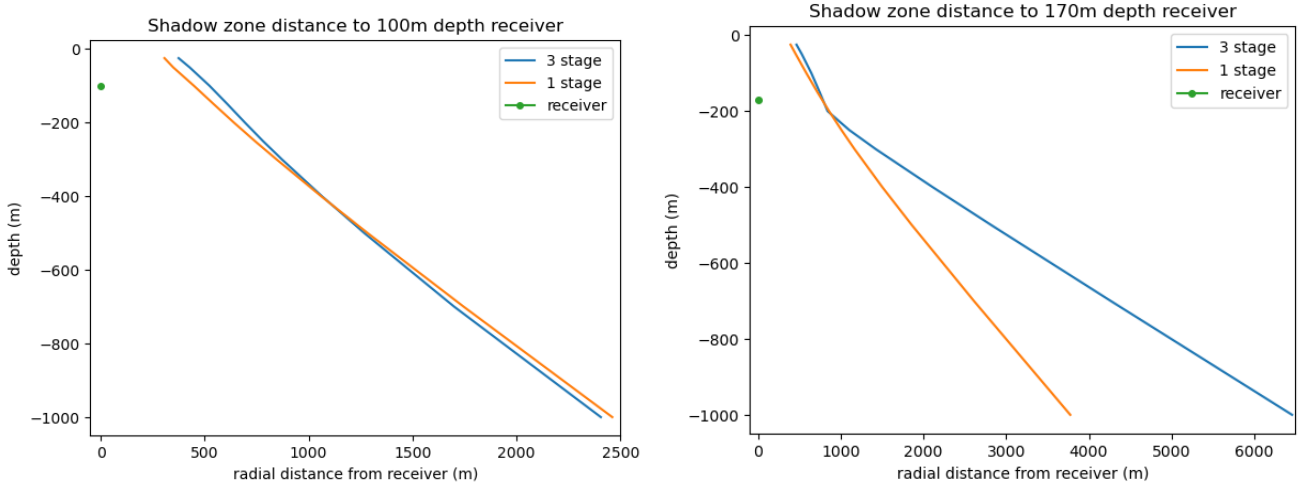

Figure 11. Example simulated shadow zone boundary (r,z) coordinates for 100 m and 170 m depth receiver antennas, for 1 stage and 3 stage n(z) profiles (see Table 1). Over the range of the SDP pulsing runs and antenna depths exceeding 100 m, the 3 stage model implies a smaller shadowed volume.

https://doi.org/10.5194/egusphere-2026-1678
Preprint. Discussion started: 8 May 2026

the two ice models for neutrino detector stations with 170 m and 100 m deep antenna deployments. The 3 stage model yields a larger effective volume than the 1 stage model at typical ARA station detector depths.

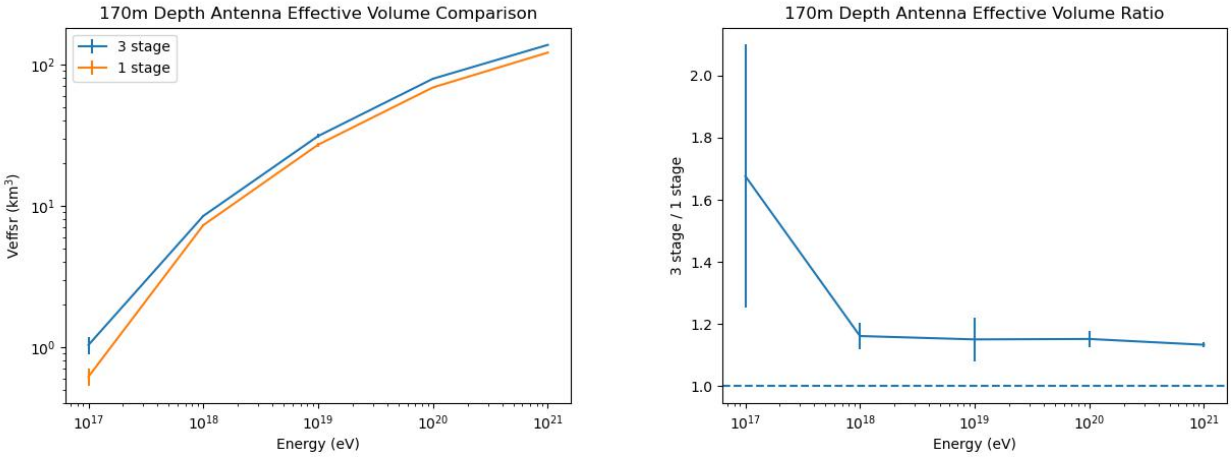

Figure 12. Simulated effective volume (left) and ratio (right) plots for refractive index profiles specified by equations (5) and (6), for neutrino energies of 10^{17}, 10^{18}, 10^{19}, 10^{20}, 10^{21} eV for 170 m depth detector typical of ARA station. Error bars shown are statistical only.

8 Conclusion

Measured dt(D,R) time differences from deep radio-frequency transmitters support a glaciologically-motivated 3 stage exponential n(z) model over 1 stage exponential model, whereas the SPICE core density measurements alone give no clear discrimination between the models. The 3 stage model is closer to converted density in the firn region, but exceeds converted density in the bubbly ice region, where the 1 stage model shows improvement. This suggests that the index of refraction may exceed that of the linear proportional relation to density at greater depths. Future analysis of the amplitude and frequency content of D and R signals can help refine the n(z) model, as phenomena such as flux focusing are also sensitive to ray curvature. A comparison of simulated shadowed zone boundaries with those extrapolated from signal amplitudes as a function of depth can also provide an independent check on the refractive index profile. An improved n(z) model should also help to provide a more accurate effective volume estimation and aid in current calibration efforts for UHEN experiments in both Greenland and the South Pole, as well as future planned experiments, such as the radio component of the IceCube-Gen2 Radio experiment.

Team list.

ARA Collaboration:

https://doi.org/10.5194/egusphere-2026-1678
Preprint. Discussion started: 8 May 2026

N. Alden (UC), S. Ali (KU), P. Allison (OSU), S. Archambault (Chiba), J.J. Beatty (OSU), D. Besson (KU), A. Bishop (UW), P. (NTU), Y.C. Chen (NTU), Y.-C. Chen (NTU), S. Chiche (ULB), B.A. Clark (UMD), A. Connolly (OSU), K. Couberly (KU), L. Cremonesi (UCL), A. Cummings (PSUigc; PSUphys; PSUast), P. Dasgupta (OSU), R. Debolt (OSU), S. de Kockere (VUB), K.D. de Vries (VUB), C. Deaconu (UC), M.A. DuVernois (UW), J. Flaherty (OSU), E. Friedman (UMD), R. Gaior (Chiba), P. Giri (UNL), J. Hanson (Whittier), N. Harty (UD), K.D. Hoffman (UMD), M.-H. Huang (NTU; NUU), K. Hughes (OSU), A. Ishihara (Chiba), A. Karle (UW), J.L. Kelley (UW), K.-C. Kim (UMD), M.-C. Kim (Chiba), I. Kravchenko (UNL), R. Krebs (PSUigc; PSUphys), C.Y. Kuo (NTU), K. Kurusu (Chiba), U.A. Latif (VUB), C.H. Liu (UNL), T.C. Liu (NTU; NPU), W. Luszczak (OSU), A. Machtay (OSU), K. Mase (Chiba), M.S. Muzio (UW; PSUigc; PSUphys; PSUast), J. Nam (NTU), R.J. Nichol (UCL), A. Novikov (UD), A. Nozdrina (OSU), E. Oberla (UC), C.W. Pai (NTU), Y. Pan (UD), C. Pfendner (Denison), N. Punsuebsay (UD), J. Roth (UD), A. Salcedo-Gomez (OSU), D. Seckel (UD), M.F.H. Seikh (KU), Y.-S. Shiao (NTU; NDL), J. Stethem (OSU), S.C. Su (NTU), S. Toscano (ULB), J. Torres (OSU), J. Touart (UMD), N. van Eijndhoven (VUB), A. Vieregg (UC), M. Vilarino Fostier (ULB), M.-Z. Wang (NTU), S.-H. Wang (NTU), P. Windischhofer (UC), S.A. Wissel (PSUigc; PSUphys; PSUast), C. Xie (UCL), S. Yoshida (Chiba), R. Young (KU)

Author contributions. Kenny Couberly was the main author of this manuscript and led the analysis discussed. The ARA Collaboration designed, constructed, and now operates the ARA detectors. Data processing and calibration, Monte Carlo simulations of the detector and of theoretical models and data analyses are performed by a large number of collaboration members, who also discussed and approved the scientific results presented here.

Competing interests. The authors declare that they have no conflict of interest

Acknowledgements. We are deeply indebted to the KU Physics and Astronomy Machine Shop, and particularly Scott Voigt and Mark Stockham, who designed and constructed the custom antenna used for recording the primary data essential to this measurement. We would like to thank IceCube and specifically the winterovers for the support in operating the detector; we also express our appreciation for the authors of the `NuRadioMC` code that was used for our simulations. We thank the Raytheon Polar Services Corporation, Lockheed Martin, and the Antarctic Support Contractor for field support and enabling our work on the harshest continent.

https://doi.org/10.5194/egusphere-2026-1678
Preprint. Discussion started: 8 May 2026

Financial support. We are thankful to the National Science Foundation (NSF) Office of Polar Programs and Physics Division for funding support. We further thank the Taiwan National Science Councils Vanguard Program NSC 92-2628-M-002-09 and the Belgian F.R.S. FNRS Grant 4.4508.01. A. Connolly thanks the NSF for Award 1806923 and also acknowledges the Ohio Supercomputer Center. S. A. Wissel thanks the NSF for support through CAREER Award 2033500. M. S. Muzio thanks the NSF for support through MPS-Ascend Postdoctoral Award 2138121. A. Vieregg thanks the Sloan Foundation and the Research Corporation for Science Advancement, the Research Computing Center and the Kavli Institute for Cosmological Physics at the University of Chicago for the resources they provided. R. Nichol thanks the Leverhulme Trust for their support. K.D. de Vries is supported by European Research Council under the European Unions Horizon research and innovation program (grant agreement 763 No 805486). D. Besson, I. Kravchenko, and D. Seckel thank the NSF for support through the IceCube EPSCoR Initiative (Award ID 2019597)

https://doi.org/10.5194/egusphere-2026-1678
Preprint. Discussion started: 8 May 2026

References

Aartsen, M. G., Abbasi, R., Ackermann, M., Adams, J., Aguilar, J., Ahlers, M., Ahrens, M., Alispach, C., Allison, P., Amin, N., et al.: IceCube-Gen2: the window to the extreme Universe, Journal of Physics G: Nuclear and Particle Physics, 48, 060 501, 2021.

Aguilar, J. A., Allison, P., Beatty, J. J., Bernhoff, H., Besson, D. Z., Bingefors, N., Botner, O., Bouma, S., Buitink, S., Carter, K., et al.: The Radio Neutrino Observatory Greenland (RNO-G), in: 37th International Cosmic Ray Conference (ICRC2021), vol. 395, 2022.

Alley, R. B. and Koci, B. R.: Ice-core analysis at site A, Greenland: preliminary results, Annals of Glaciology, 10, 1–4, 1988.

Allison, P., Bard, R., Beatty, J., Besson, D. Z., Bora, C., Chen, C.-C., Chen, C.-H., Chen, P., Christenson, A., Connolly, A., et al.: Performance of two Askaryan Radio Array stations and first results in the search for ultrahigh energy neutrinos, Physical Review D, 93, 082 003, 2016.

Allison, P., Archambault, S., Beatty, J., Besson, D., Chen, C., Chen, C., Chen, P., Christenson, A., Clark, B., Clay, W., et al.: Long-baseline horizontal radio-frequency transmission through polar ice, Journal of Cosmology and Astroparticle Physics, 2020, 009, 2020.

Bader, H.: Sorge's Law of densification of snow on high polar glaciers, Journal of Glaciology, 2, 319–323, 1954.

Casey, K. A., Fudge, T., Neumann, T., Steig, E., Cavitte, M., and Blankenship, D.: The 1500 m South Pole ice core: recovering a 40 ka environmental record, Annals of Glaciology, 55, 137–146, 2014.

Cumming, W.: The dielectric properties of ice and snow at 3.2 centimeters, Journal of Applied Physics, 23, 768–773, 1952.

Evans, S.: Dielectric properties of ice and snow–a review, Journal of Glaciology, 5, 773–792, 1965.

Gavin, H. P.: The Levenberg-Marquardt algorithm for nonlinear least squares curve-fitting problems, Department of Civil and Environmental Engineering Duke University August, 3, 2019.

Glaser, C., García-Fernández, D., Nelles, A., Alvarez-Muñiz, J., Barwick, S. W., Besson, D. Z., Clark, B. A., Connolly, A., Deaconu, C., de Vries, K., et al.: NuRadioMC: Simulating the radio emission of neutrinos from interaction to detector, The European Physical Journal C, 80, 1–35, 2020.

Gow, A., Meese, D., Alley, R., Fitzpatrick, J., Anandakrishnan, S., Woods, G., and Elder, B.: Physical and structural properties of the Greenland Ice Sheet Project 2 ice core: A review, Journal of Geophysical Research: Oceans, 102, 26 559–26 575, 1997.

Hawley, R. L. and Morris, E. M.: Borehole optical stratigraphy and neutron-scattering density measurements at Summit, Greenland, Journal of Glaciology, 52, 491–496, 2006.

Hawley, R. L., Morris, E. M., and McCONNELL, J. R.: Rapid techniques for determining annual accumulation applied at Summit, Greenland, Journal of Glaciology, 54, 839–845, 2008.

Herron, M. M. and Langway, C. C.: Firn densification: an empirical model, Journal of Glaciology, 25, 373–385, 1980.

Kovacs, A., Gow, A. J., and Morey, R. M.: The in-situ dielectric constant of polar firn revisited, Cold Regions Science and Technology, 23, 245–256, 1995.

Latif, U. A.: Towards Measurement of UHECR with the ARA Experiment, Ph.D. thesis, University of Kansas, 2020.

Lipenkov, V. Y., Salamatin, A. N., and Duval, P.: Bubbly-ice densification in ice sheets: II. Applications, Journal of Glaciology, 43, 397–407, 1997.

Robin, G. d. Q., Evans, S., and Bailey, J. T.: Interpretation of radio echo sounding in polar ice sheets, Philosophical Transactions of the Royal Society of London. Series A, Mathematical and Physical Sciences, 265, 437–505, 1969.

Salamatin, A. N., Lipenkov, V. Y., and Duval, P.: Bubbly-ice densification in ice sheets: I. Theory, Journal of Glaciology, 43, 387–396, 1997.

Schytt, V.: Snow Studies at Maudheim: Snow Studies Inland: the Inner Structure of the Ice Shelf at Maudheim as Shown by Core Drilling, 1958.

https://doi.org/10.5194/egusphere-2026-1678
Preprint. Discussion started: 8 May 2026

Stevens, C. M., Verjans, V., Lundin, J., Kahle, E. C., Horlings, A. N., Horlings, B. I., and Waddington, E. D.: The community firn model (cfm) v1. 0, Geoscientific Model Development, 13, 4355–4377, 2020.

Welling, C. and Collaboration, T. R.-G.: Brief communication: Precision measurement of the index of refraction of deep glacial ice at radio frequencies at Summit Station, Greenland, The Cryosphere, 18, 3433–3437, 2024a.

Welling, C. and Collaboration, T. R.-G.: Precision measurement of the index of refraction of deep glacial ice at radio frequencies at Summit Station, Greenland, The Cryosphere, 2024b.

Winchen, T.: RadioPropa — A Modular Raytracer for In-Matter Radio Propagation, EPJ Web of Conferences, 216, 03 002, https://doi.org/10.1051/epjconf/201921603002, 2019.